ADVANCED ELECTRONIC MATERIALS
www.advelectronicmat.de

Tuning Ni/Al Ratio to Enhance Pseudocapacitive Charge Storage Properties of Nickel–Aluminum Layered Double Hydroxide

Gengnan Li, Xianghui Zhang, Dantong Qiu, Zilin Liu, Chen Yang, Cody B. Cockreham, Baodong Wang, Liangjie Fu, Jianghao Zhang, Berlin Sudduth, Xiaofeng Guo, Hui Sun, Zhangyi Huang, Jianqi Qi, Junming Sun, Su Ha, Yong Wang, and Di Wu**

Compared with batteries, the advantages of capacitive energy storage include high power, fast charging kinetics, and long cycling stability. Owing to their layered structure and tunable transition metal charge, layered double hydroxides (LDHs) have great potential to be applied as pseudocapacitor materials. Here, a systematic experimental study is reported on the impact of the Ni/Al ratio on the structure, morphology, ion transport kinetics, interlayer phenomena, and performance of NiAl-LDH supercapacitor electrode materials, in which three NiAl-LDH materials with Ni/Al ratios of 2, 3, and 4, are synthesized using a hydrothermal method. The increase of the Ni/Al ratio results in more open interlayer space resulting in faster ion diffusion kinetics. Although an increase in the Ni/Al ratio introduces more redox active sites, it leads to degradation in crystallinity and morphology, which has a significant negative impact on pseudocapacitance. Electrochemical tests suggest that at Ni/Al = 3, the NiAl-LDH electrode exhibits optimum specific capacitance of 2128 F g^{-1} at 1 A g^{-1} with long cycle stability. This work highlights the complex interplay among compositional and structural factors on the kinetic and performance behaviors of NiAl-LDH materials. Subtle compositional modification is an effective strategy to enhance the pseudocapacitive charge storage property of NiAl-LDH pseduocapacitor materials.

1. Introduction

Electrochemical capacitors and rechargeable batteries are two major types of electrochemical energy storage devices, which share promising futures in mitigating the existing global scale energy crisis.[1–7] Capacitive energy storage devices take advantage of electrostatic storage of charges at or near the surface of the electrode material, which is not involved in any phase transitions or solid-state reactions. Compared with rechargeable batteries, electrochemical capacitors feature advantages such as higher power density, longer cycle life, a much faster charge–discharge process, and better reversibility. Typically, electrochemical capacitors are classified into two categories: electrical double-layer capacitors (EDLCs) and pseudocapacitors. EDLCs store electrical energy through formation of an ionic double layer at and near the electrode–electrolyte interfaces.

Dr. G. Li, X. Zhang, D. Qiu, C. Yang, C. B. Cockreham, Prof. X. Guo, Prof. D. Wu
Alexandra Navrotsky Institute for Experimental Thermodynamics
Washington State University
Pullman, Washington 99163, USA
E-mail: d.wu@wsu.edu

Dr. G. Li, X. Zhang, C. Yang, C. B. Cockreham, J. Zhang, B. Sudduth, Prof. J. Sun, Prof. S. Ha, Prof. Y. Wang, Prof. D. Wu
The Gene and Linda Voiland School of Chemical Engineering and Bioengineering
Washington State University
Pullman, Washington 99163, USA

D. Qiu, Prof. X. Guo, Prof. D. Wu
Materials Science and Engineering
Washington State University
Pullman, Washington 99163, USA

Z. Liu, Dr. B. Wang
National Institute of Clean-and-Low-Carbon Energy
Beijing 102211, China
E-mail: wangbaodong@nicenergy.com

Dr. L. Fu
Centre for Mineral Materials
School of Minerals Processing and Bioengineering
Central South University
Changsha, Hunan 410083, China

Prof. X. Guo, Prof. D. Wu
Department of Chemistry
Washington State University
Pullman, Washington 99163, USA

Prof. H. Sun
Petroleum Processing Research Center
East China University of Science and Technology
Shanghai 200237, China

Prof. H. Sun
International Joint Research Center of Green Energy Chemical Engineering
East China University of Science and Technology
Shanghai 200237, China

Z. Huang, Prof. J. Qi
College of Physical Science and Technology
Sichuan University
Chengdu 610064, China

The ORCID identification number(s) for the author(s) of this article can be found under https://doi.org/10.1002/aelm.201900215.

DOI: 10.1002/aelm.201900215

© 2019 WILEY-VCH Verlag GmbH & Co. KGaA, Weinheim

Although they have higher power, longer cycle life, and faster charge–discharge kinetics than Li-ion batteries, application of EDLCs suffer from their intrinsically low energy density.[8–11] Pseudocapacitive energy storage mechanism takes advantage of fast and reversible Faradic redox reactions at or near the surface of the electrochemically active material within an appropriate potential range.[12–17] Compared with carbon-based EDLC materials, pseudocapacitive materials, such as conducting polymers (CPs) and transition metal oxides/hydroxides/sulfides, feature significantly higher energy density and higher specific capacitance.[18–28]

2D (Co and Ni)-based monometallic hydroxides were reported to have high pseudocapacitance. However, they suffer from severe thermodynamic metastability resulting in phase degradation and transition, which negatively impact the pseudocapacitance. One strategy is to substitute these hydroxides with their bimetallic counterparts, namely, transition metal layered double hydroxides (LDHs), which contain Mn, Fe, Co, Ni, Cu, and/or Zn.[29–32] These LDHs have greatly enhanced structural stability, tunable transition metal charge, and high pseudocapacitance, while maintaining the 2D open layered structure.

As an inorganic anion conductor, LDH structure features charged brucite-like metal hydroxide layers consisting of octahedra centered with divalent (M^{2+}) and trivalent (M^{3+}) metal ions (see **Figure 1**a). Substitution of M^{3+} for M^{2+} results in positive layer-possessed charges and intercalation of negative charge-balancing ions (A^{n-}), such as carbonate species, within the accessible interlayer gallery. The interlayer confined guest species include anions and molecules without charge, such as water, which play crucial role in ion conduction.[4,33–35] The integration of open 2D structure and anion exchange property lead to high electron/ion transport efficiency and kinetics during the charge–discharge process. In the Faradic redox reaction, intercalation of electrolyte ions induces transition metal oxidation state (valence) evolution within the LDH layers. Such

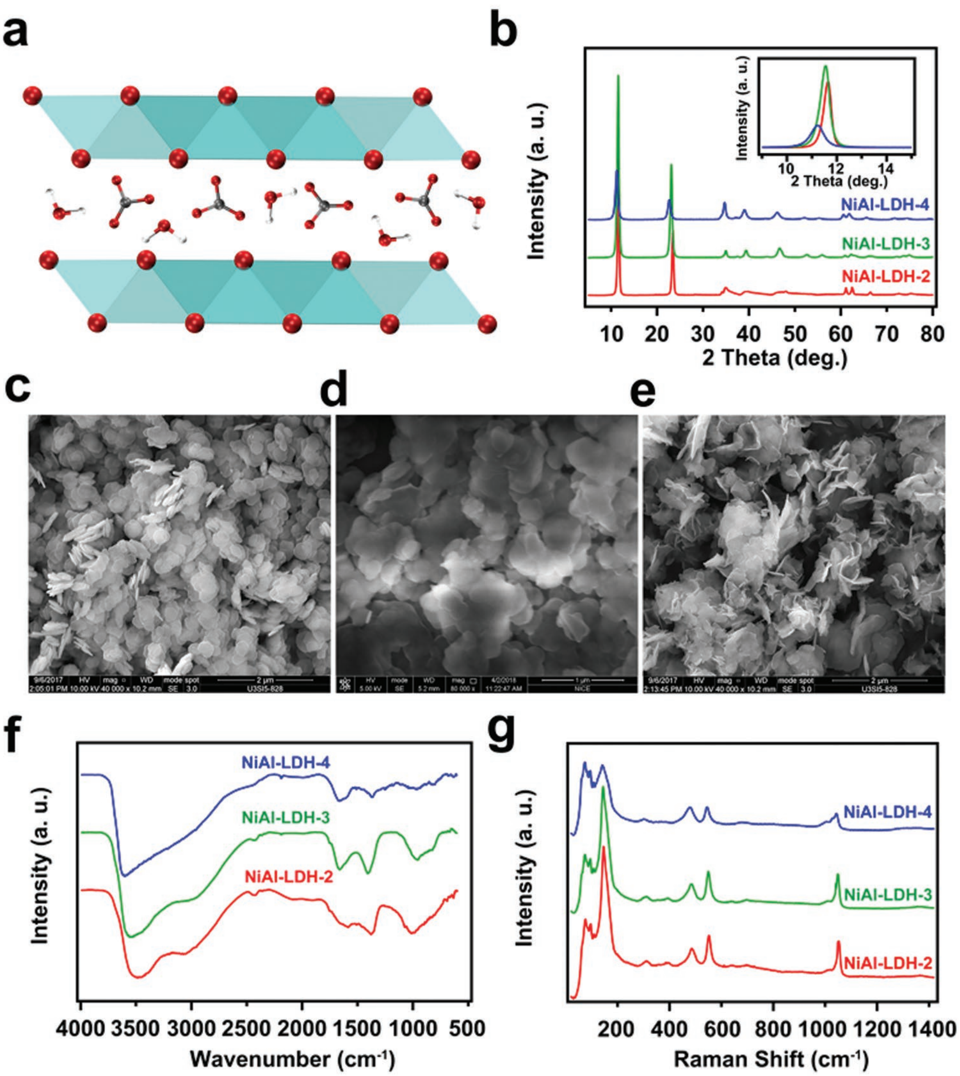

Figure 1. a) Crystal structure of NiAl-LDH. b) XRD patterns of NiAl-LDHs with different Ni/Al ratios. The inset highlights left-shift and broadening of (003) peaks as the Ni/Al ratio increases. SEM images of c) NiAl-LDH-2, d) NiAl-LDH-3, and e) NiAl-LDH-4. f) DRIFTS and g) Raman spectra of NiAl-LDHs with different Ni/Al ratios.

working mechanism highlights the compositional factors such as the M^{2+}/M^{3+} ratio, which determines the number of layer-possessed charge and LDH conductivity; and reaction kinetics, such as the electrolyte ion diffusion, in which strong ion diffusion resistance (low ion diffusion rate) in the LDH gallery leads to poor utilization of the inner active surface and inferior rate capability.[12,36,37] Numerous studies have been carried out to increase the specific capacity of LDH materials; however, systematic and fundamental studies on the impacts of the M^{2+}/M^{3+} ratio on the structure, intercalated species–layer interactions, charge–discharge kinetics, and electrochemical performance of LDHs as pseudocapacitive charge storage materials are very few.[12,36,37]

Here, we report a comprehensive study that elucidates the impacts of the Ni/Al ratio on the structure, morphology, interfacial phenomena, cycle stability, and performance of NiAl-LDH as a pseudocapacitive charge storage material. Variation of the Ni/Al ratio from 2 to 4 significantly modifies the specific capacity, and results in lower crystallinity and faster kinetics. Integration of all the experimentally determined results using a spectrum of analytical techniques reveals the composition–structure–performance relationships of NiAl-LDHs. The fundamental understanding gained from this study may provide a general guidance to rational design of LDH-based supercapacitors with high charge–discharge capability and enhanced stability by tuning compositional factors.

2. Results

The inductively coupled plasma-mass spectrometry (ICP-MS) results (see **Table 1**) suggest that the molar ratios of Ni/Al in the as-synthesized LDHs are 2.08, 2.69, and 3.52 for NiAl-LDH-2, 3, and 4, respectively. This is in good agreement with the reactant contents used during material synthesis.

Table 1. Compositional and structural parameters of all NiAl-LDH samples studied.

Sample	Molar formula of NiAl-LDH[a]	*hkl* = *003*		*hkl* = *110*		Lattice parameters		
	$[Ni^{2+}{}_{n}\,Al^{3+}(OH^-)_x](CO_3{}^{2-})_y(H_2O)_z$	2θ [°]	d [Å]	2θ [°]	d [Å]	a [Å][b]	c [Å][c]	Basal spacing [Å][d]
NiAl-LDH-2	$[Ni^{2+}{}_{2.08}\,Al^{3+}(OH^-)_{4.82}](CO_3{}^{2-})_{1.17}(H_2O)_{0.46}$	11.60	7.62	61.13	1.51	3.02	22.86	7.62
NiAl-LDH-3	$[Ni^{2+}{}_{2.69}\,Al^{3+}(OH^-)_{5.77}](CO_3{}^{2-})_{1.30}(H_2O)_{0.91}$	11.54	7.66	60.89	1.52	3.04	22.98	7.66
NiAl-LDH-4	$[Ni^{2+}{}_{3.52}\,Al^{3+}(OH^-)_{6.45}](CO_3{}^{2-})_{1.80}(H_2O)_{1.01}$	11.20	7.90	60.53	1.53	3.06	23.70	7.90

[a] From coupled ICP-MS and TG-DSC-MS analyses; [b] From the (110) reflection of XRD patterns, $a = 2d_{110}$; [c] From the (003) reflections of XRD patterns, $c = 3d_{003}$; [d] Basal spacing = d_{003}.

The powder X-ray diffraction (XRD) patterns of NiAl-LDHs are presented in Figure 1b. The positions of diffraction peaks suggest that all samples share a hexagonal structure (PDF# 15-0087) without other impurity phases. The *a*-parameter, which is related to the average cation–cation distance within each layer, can be calculated according to $a = 2 \times d_{110}$. The *c*-parameter can be derived from the (003) reflection using equation $c = 3 \times d_{003}$, which provides the thickness of the layer and interlayer distance. In addition, the basal spacing of ≈7.6 Å obtained is characteristic of brucite-type phases with carbonate anions intercalated (Table 1).[38] The scanning electron microscope (SEM) images presented in Figure 1c–e reveal the NiAl-LDH morphologies. Specifically, NiAl-LDH-2 shows hexagonal platelet layer morphology with a mean lateral size of ≈250 nm and a thickness of ≈50 nm. In contrast, NiAl-LDH-3 and 4 are in the form of layers without clearly defined asymmetric shape. In addition, elemental mapping analyses clearly reveal that Ni, Al, and O elements distribute uniformly within these NiAl-LDH samples (see Figures S1–S3, Supporting Information).

Figure 1f presents the diffuse reflectance infrared Fourier transform spectroscopy (DRIFTS) spectra of NiAl-LDH samples. The broad absorption peak at ≈3500 cm^{-1} corresponds to the O–H stretching vibration of hydroxyl groups of the brucite-layer and the surface-sorbed water molecules. The absorption at ≈3070 cm^{-1} is attributed to the hydrogen bonds between interlayer water molecules and carbonate ions, which becomes weaker as the Ni/Al ratio increases. The band at ≈1650 cm^{-1} is ascribed to the bending vibration of adsorbed water molecules. The peaks at ≈1365 and ≈1000 cm^{-1} reflect the asymmetric stretching of interlayer carbonate ions. The bands between 900 and 600 cm^{-1} are related to the lattice vibration of M–O, M–O–M, and O–M–O.[39–41]

Raman spectroscopy data are shown in Figure 1g to elucidate the low-frequency modes in the NiAl-LDHs. The strongest peaks at ≈150 cm^{-1} are associated with the O–M–O bending modes. The bands between 200 and 300 cm^{-1} are relatively weak, owing to the hydrogen bond formation between hydroxyl groups of the brucite-like layers and the interlayer anions.[42,43] The bands at about 480 cm^{-1} are due to the symmetric stretching of bonds in the M(II)–O–M(III) structure,[44,45] which exhibit lower Raman shift as the Ni/Al ratio increases. The peaks at ≈550 cm^{-1} correspond to stretching of OH–O bands between the carbonate ions and interlayer water molecules. The vibration at about 1050 cm^{-1} is related to the $CO_3{}^{2-}$ symmetric stretching mode.[46]

To further determine the surface compositions and metal oxidation states of NiAl-LDHs, X-ray photoelectron spectroscopy (XPS) measurements were performed. The survey spectra in **Figure 2**a suggest that all NiAl-LDH samples are composed of Ni, Al, C, and O. The Ni 2p spectra show two typical Ni^{2+} $2p_{3/2}$ and $2p_{1/2}$ peaks centered at 856.2 and 873.8 eV, respectively. The spin energy separation observed (17.6 eV) is characteristic of Ni^{2+} in $Ni(OH)_2$. Additionally, the other two signals at lower binding energy correspond to the satellite peaks of Ni^{2+} $2p_{3/2}$ and $2p_{1/2}$[41,47,48] (Figure 2b). For the C1s spectra, the peaks at 284.8 and 288.8 eV are assigned to C–C and C–O bands, respectively. The sharp peaks at ≈288.8 eV strongly suggest the existence of functional groups containing C–O bonds in the NiAl-LDH samples studied[36,49,50] (Figure 2c). There is merely

© 2019 WILEY-VCH Verlag GmbH & Co. KGaA, Weinheim

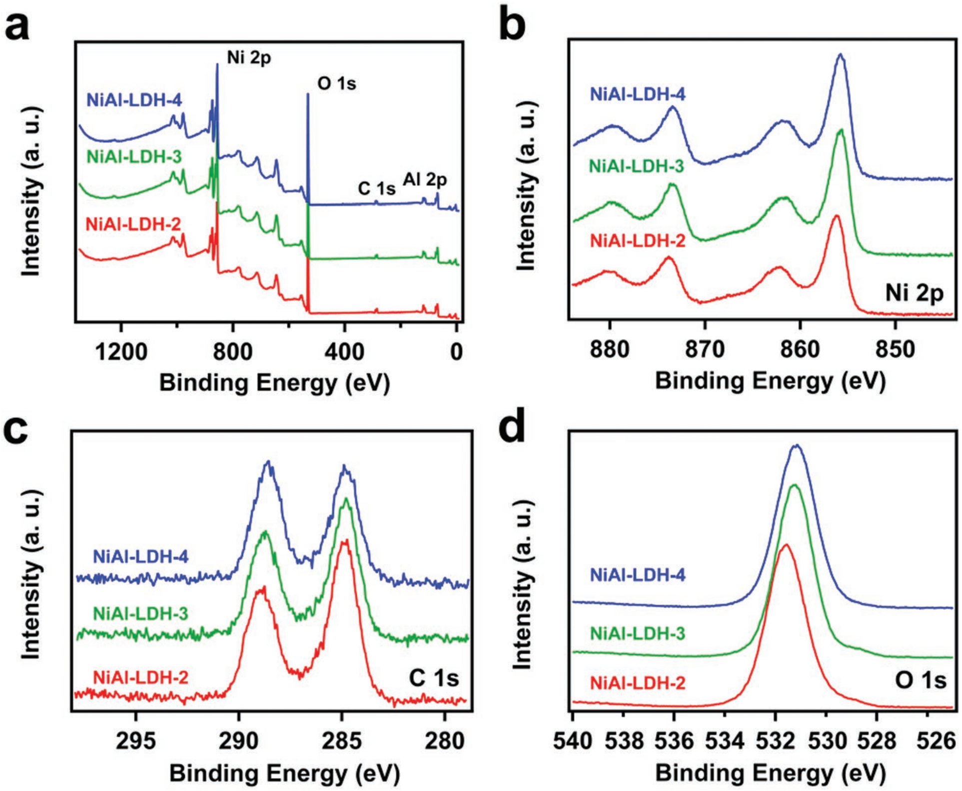

Figure 2. a) XPS survey, b) Ni 2p, c) C1s, and d) O 1s spectra of NiAl-LDH-2, 3, and 4.

a single peak at about 531.6 eV observed in the O 1s spectrum of each sample, which corresponds to the lattice oxygen species[50,51] (Figure 2d). Moreover, as the Ni/Al ratio increases, the binding energies of Ni 2p, O 1s, and C 1s shift to lower values. Such binding energy shifts are related to the dispersion states of Ni^{2+} and Al^{3+} species and the oxidation states of these elements.[51,52] As expected, the intensity of Ni 2p peak increases as the Ni/Al ratio increases, while the C 1s intensity decreases, which indicates a decrease in interlayer carbonate ion population. Such phenomenon is in excellent accordance with the peak intensity decreases observed from DRIFTS (≈3070 cm^{-1}) and Raman spectroscopy (1050 cm^{-1}) data (see Figure 1f,g).

The thermogravimetric-differential scanning calorimetry-mass spectrometer (TG-DSC-MS) data are presented in **Figure 3**. Two-stage TG curve is observed for each sample, which is in excellent agreement with the multievent DSC (endothermic) and MS profiles. According to the MS data, the relatively broad DSC peaks at lower temperatures, centered at 265.3 °C for NiAl-LDH-2, 240.1 °C for NiAl-LDH-3, and 169.0 °C for NiAl-LDH-4, correspond to dehydration of interlayer confined H_2O (m/z = 18). In addition, the DSC signals at higher temperatures, centered at 375.3 °C for NiAl-LDH-2, 360.1 °C for NiAl-LDH-3, and 345.0 °C for NiAl-LDH-4, are associated with simultaneous evolution of H_2O and CO_2 (m/z = 18 and 44). The shape and width of MS peaks mirror corresponding DSC signals (see Figure 3). The simultaneous coevolution of H_2O and CO_2 probably suggests that either the charge-balancing carbonate species interact strongly with water or hydroxyls, or the carbonate species are in the form of bicarbonate ions. As the Ni/Al increases, both the low and high temperature peaks shift to lower temperatures. On the other hand, this set of TG-DSC-MS results provides the compositional basis to quantify the content of H_2O and carbonate species, and suggests a complex chemical environment for the interlayer confined (intercalated) H_2O and carbonate species. Coupled with results from ICP-MS analysis, we are able to determine the stoichiometries (molar formula) of all three NiAl-LDH samples (see Table 1).

The electrochemical properties for NiAl-LDH samples were thoroughly evaluated. Chemically, during the pseudocapacitance redox reactions, the OH^- ions in the KOH electrolyte intercalate in to the interlayer space of NiAl-LDH and interact with the interlayer-confined H_2O and CO_3^{2-} to induce the valence evolution of Ni^{2+} in the host layer, when a cathodic potential is applied.

$$NiAl-LDH+OH^- \rightarrow LDH-NiOOH+H_2O+e^- \quad (1)$$

Disinsertion of OH^- ions takes place once an anodic potential is placed, in which oxidation reaction occurs.

$$LDH-NiOOH+H_2O+e^- \rightarrow NiAl-LDH+OH^- \quad (2)$$

The cyclic voltammograms (CV curves) with potential ranging from 0.0 to 0.6 V demonstrate that all three NiAl-LDH samples have two pairs of redox peaks. These peaks are clearly observed even at a high scan rate of 100 mV s^{-1}. This is strong evidence suggesting pseudocapacitive nature with fast response. Meanwhile, the peak current increases gradually and the anodic peaks shift to more positive potential, while the cathodic peaks shift to more negative potential. Such phenomena are

© 2019 WILEY-VCH Verlag GmbH & Co. KGaA, Weinheim

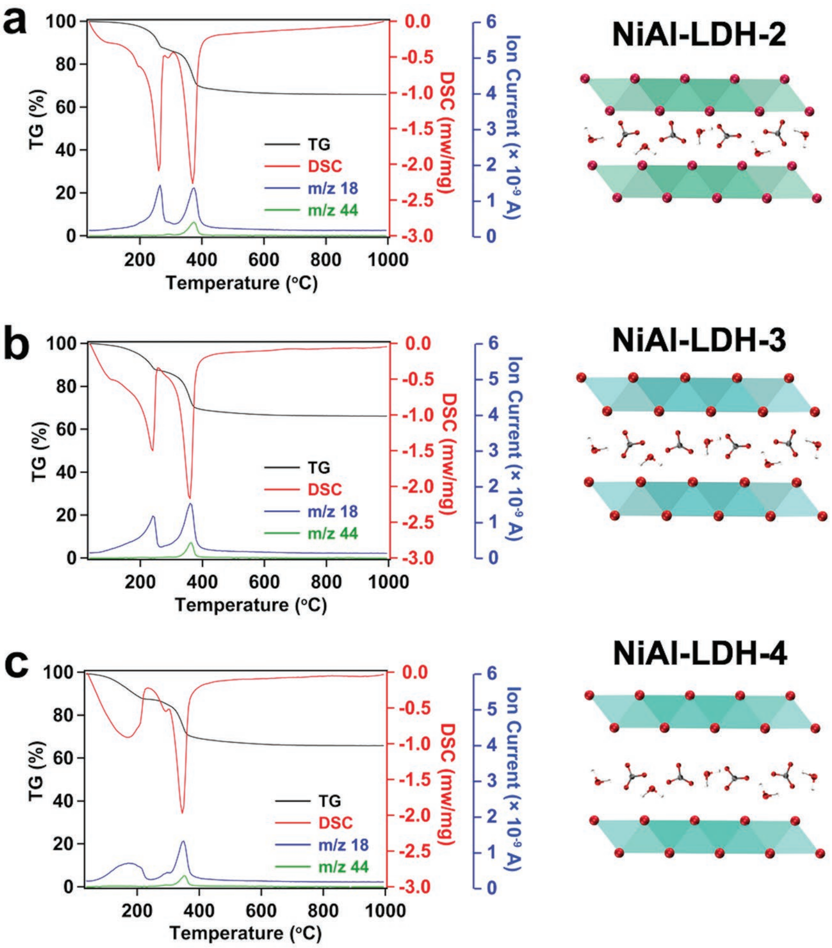

Figure 3. TG-DSC-MS curves of NiAl-LDHs with different Ni/Al ratios: a) NiAl-LDH-2, b) NiAl-LDH-3, and c) NiAl-LDH-4.

ascribed to the increase of internal diffusion resistance of the electrodes.[37] Moreover, the cathodic peak current density is a linear function of the square root of the applied scan rate ($v^{1/2}$) (see **Figure** 4), which suggests that the Faradic reaction is mainly determined by the intercalation–deintercalation of ions and the redox surface reactions taking place in the charge storage process.[53] The CV curve of NiAl-LDH-3 encircles the largest area among all three electrode materials, suggesting the highest specific capacitance.

Figure 5a–c presents the galvanostatic charge–discharge (GCD) profiles (0.0–0.4 V) of the NiAl-LDH electrodes at a series of current densities. The nonlinear sections of the discharge curves demonstrate typical pseudocapacitance behavior, which is due to quasi-reversible redox at the electrode surface. These nearly symmetric curves suggest highly reversible charge–discharge process and electrochemical capacitive behavior. In addition, all electrode materials studied present two discharge plateaus, which is consistent with the CV analysis results. In Figure 5d, the specific capacitances (F g^{-1}) of all NiAl-LDH electrode materials are plotted against current density. Notably, NiAl-LDH-3 presents the highest specific capacitance observed throughout the whole current density range, which suggests high capacity for fast energy storage and delivery. This is in excellent agreement with the result from CV analysis (see Figure 4). At 1 A g^{-1}, NiAl-LDH-3 shows the optimum specific capacitance of 2128 F g^{-1}. Between the other two samples, below 10 A g^{-1}, NiAl-LDH-2 has higher specific capacitance, while NiAl-LDH-4 shows higher values when the current density exceeds 10 A g^{-1}. **Table 2** presents a summary of pseudocapacitive performance of NiAl-LDH-based materials reported elsewhere, in which the specific capacities of materials studied in this work are also listed.

Figure 6a presents the electrochemical impedance spectra (EIS) data of all NiAl-LDH samples. EIS plots provide critical insights into the ion transport and charge storage kinetics at the electrode/electrolyte interfaces. Typically, each EIS curve features two regions as a function of frequency, which are associated with the resistance phenomena during the interfacial processes of Faradic reactions. In the high-frequency region (100k–15 Hz), the intercept at the real axis (Z') is series resistance, R_s, which represents the integrated resistance of electrode, electrolyte, electrode material/liquid electrolyte interface, and the resistance at the Ni foam electrode–active material interfaces.[58] In this study, the NiAl-LDH-3 electrode shows the lowest R_s value (see the inset of Figure 6a). On the other hand, in the low-frequency region (15–0.01 Hz), the slope of the linear line corresponds to Warburg impedance (W), which is related to the electrolyte ion diffusion in the electrode. NiAl-LDH-4 presents the steepest slope among all the three electrodes, indicating the lowest diffusion resistance. The coulombic efficiency (η) of the charge storage process was derived to evaluate the quality of charge/ion transfer during the electrochemical reaction (see Figure 6b). All three NiAl-LDH electrodes exhibit high coulombic efficiency, above 80% during 1000 cycles.

3. Discussions

Typical layered double hydroxide is composed of neutral brucite-like host layers, $M(OH)_2$. These layers become positively charged when divalent cations (M^{2+}) are replaced by trivalent cations (M^{3+}), which are charge-balanced by anionic guest species intercalated within the interlayer space. Other than the embedded hydroxyl groups on the LDH layers, the guest species confined in the interlamellar region include carbonate species, water molecules, and OH^- of the electrolyte. Increase in Ni/Al ratio leads to significant modifications in the structural and chemical properties and the electrochemical performance of NiAl-LDH as a pseudocapacitance electrode material. The

© 2019 WILEY-VCH Verlag GmbH & Co. KGaA, Weinheim

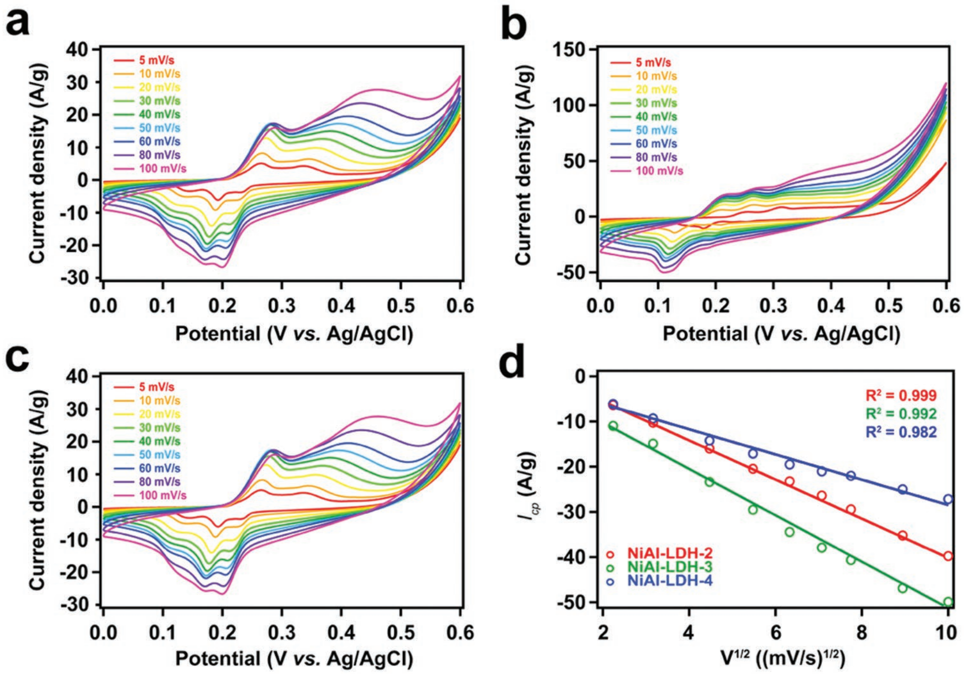

Figure 4. Cyclic voltammograms (CV curves) of NiAl-LDHs with different Ni/Al ratios at different scan rates: a) NiAl-LDH-2, b) NiAl-LDH-3, and c) NiAl-LDH-4; and d) the cathodic peak current (I_{cp}) as a function of the square root of scan rate ($\nu^{1/2}$).

structural and chemical evolutions and their impacts in the ion transport kinetics and storage capacity of NiAl-LDH electrodes are discussed below.

Generally, for layered pseudocapacitive materials, structural modifications are reflected by their electrochemical performance. During the redox reactions of the charge–discharge process, intercalation of OH^- ions of the KOH electrolyte into the NiAl-LDH interlayer space induces valence changes among Ni in the layer. First of all, increase in the vdW gap of NiAl-LDH is observed as the Ni/Al ratio increases,

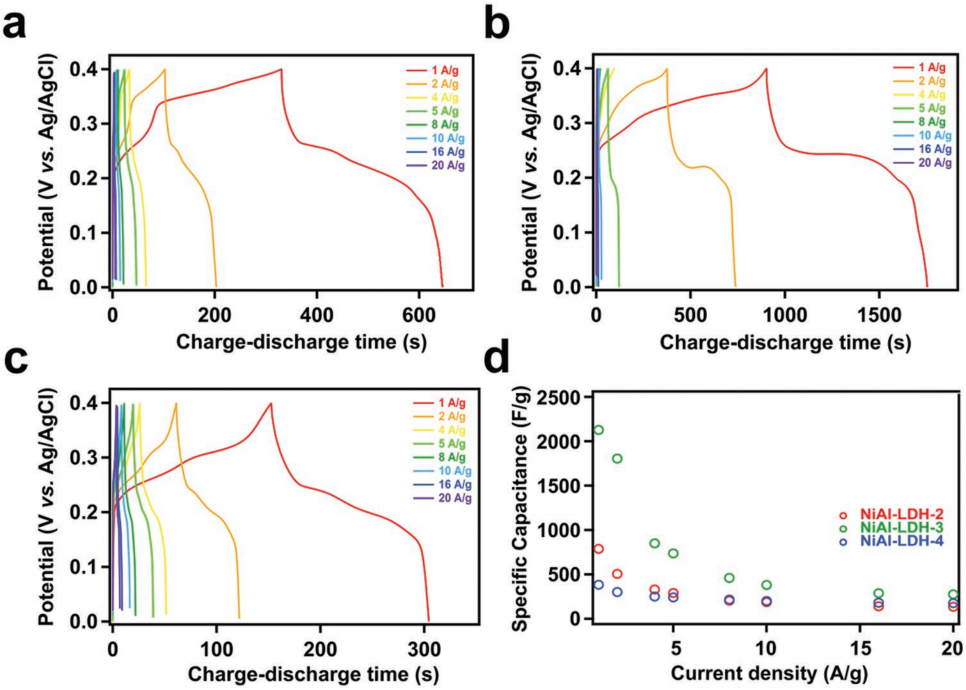

Figure 5. Galvanostatic charge–discharge (GCD) curves of NiAl-LDHs with different Ni/Al ratios at different scan rates: a) NiAl-LDH-2, b) NiAl-LDH-3, and c) NiAl-LDH-4; and d) specific capacitances of NiAl-LDH samples as current density varies.

© 2019 WILEY-VCH Verlag GmbH & Co. KGaA, Weinheim

Table 2. A Summary of Pseudocapacitive Performance of NiAl-LDH-based Materials.

Material	Capacitance [F g^{-1}]	Reference
NiAl-LDH, petal-shaped nanosheets	≈750	[54]
NiAl-LDH, hollow microsphere	1578	[55]
NiAl-LDH, petal-like	1740.5	[56]
NiAl-LDH, GNS	781.5	[57]
NiAl-LDH-2	788	*This work*
NiAl-LDH-3	2128	*This work*
NiAl-LDH-4	383	*This work*

which leads to enhanced charge storage kinetics. The inset of Figure 1 highlights the left-shift of the XRD peak at about 11.5°, which corresponds to the (003) reflection. Accordingly, the basal spacing, d_{003}, increases from 7.62 Å for NiAl-LDH-2 to 7.90 Å for NiAl-LDH-4. Moreover, Ni/Al ratio increase leads to less layer-possessed positive charge, consequently, reducing the population of anionic carbonate species confined within the interlayer space, and leading to weaker layer–OH$^-$ electrostatic interactions supported by the XRD, DRIFTS, Raman, and TG-DSC-MS data.[51] The vibration modes of water molecules, carbonate anion species, and layer-possessed hydroxyls are elucidated by DRIFTS and Raman spectroscopy. The Raman peaks at lower wavenumber (1000, 1015 cm^{-1}) are assigned to the "free" carbonate species, which are bonded to neither brucite-like layers nor interlayer water. Peaks at higher wavenumber (1050 cm^{-1}) represent carbonate species forming strong hydrogen bonds with water molecules.[43,46] We found that as the Ni/Al ratio increases, the NiAl-LDH bands shift to lower wavenumbers suggesting the presence of carbonate ions with enhanced mobility. Consequently, for NiAl-LDH-4, the DRIFTS signal at about 3070 cm^{-1}, which is attributed to the hydrogen bonding between intercalated water and carbonate ions, nearly disappears.[59] This suggests very weak carbonate–water interactions due to low concentration of layer-possessed positive charges. In addition, the Raman band at ≈480 cm^{-1}, related to the M(II)–O–M(III) bond within the LDH host layers, shifts to lower wavenumbers as the Ni/Al ratio increases, suggesting the presence of hydroxyl groups with longer O–H bond on the NiAl-LDH layers compared with the hydroxyls on the neutral brucite-like layer of Ni(OH)$_2$. Such O–H bond length increase is primarily due to decreased electrostatic attraction generated by the introduction of trivalent cations (M^{3+}) into the host layer. According to the TG-DSC-MS results, although we suspect that the interlayer charge-balancing carbonate species exist in the form of bicarbonate ions (see Figure 3), the absence of a sharp bicarbonate OH bending absorbance at ≈1220 cm^{-1} in the DRIFTS spectra suggests that it is very likely there is no interlayer confined bicarbonate ion. Further evidences from spectroscopic and computational studies are needed to test this hypothesis.

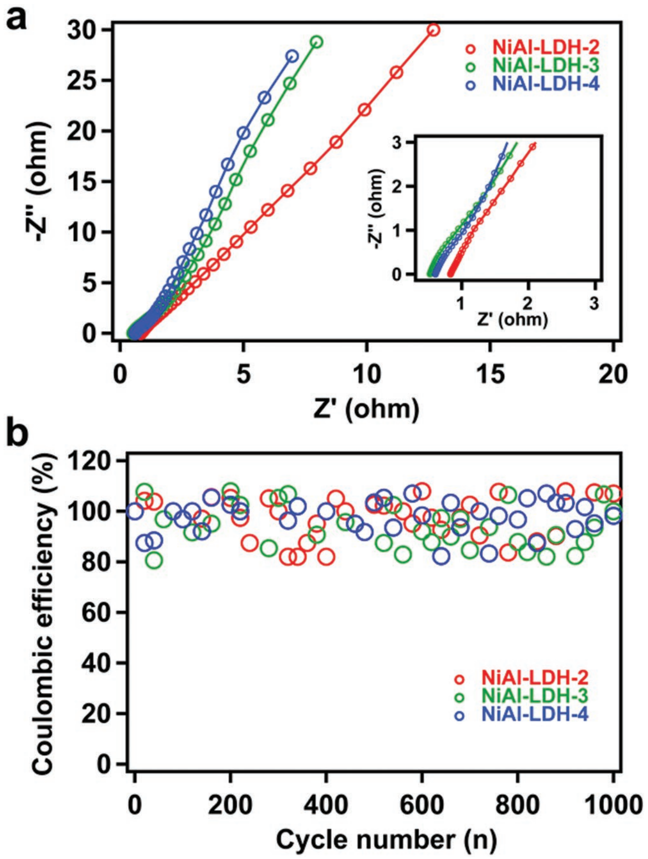

Figure 6. a) Electrochemical impedance spectra of NiAl-LDHs with different Ni/Al ratios under the influence of an AC voltage of 5 mV. The inset highlights data in the high-frequency range. b) Coulombic efficiency (η) derived from the charge–discharge cycles for NiAl-LDHs with different Ni/Al ratios (5 A g^{-1}).

To ensure better OH$^-$ ion transport kinetics, i) more open interlayer space, and ii) lower interlayer diffusion resistance from other intercalated species, such as water and carbonate ions, are necessary. With larger interlayer spacing (vdW gap) for OH$^-$ ion diffusion and lower diffusion resistance owing to less charge-balancing cation population, here, we demonstrate that NiAl-LDH-4 has faster ion transport kinetics compared with the other two samples (see Table 1). This is confirmed by the EIS data, in which NiAl-LDH-4 presents the steepest slope within the lower frequency region (Figure 5).

On the other hand, the specific capacity of NiAl-LDH is dictated by the interplay between redox site concentration and material crystallinity. Although increase in Ni/Al introduces more Ni redox reaction sites, it results in significant NiAl-LDH structural and morphological degradations, directly evidenced by the broadening of (003) peaks in the XRD patterns (Figure 1b) and the less uniform particle shape and size observed in the SEM images (Figure 1c–e). The highest specific capacity of 2128 F g^{-1} observed in this study on NiAl-LDH-3 highlights the subtle interplay between redox site concentration and surface crystallinity. Moreover, decreased layer orderliness is also revealed by the TG-DSC-MS data. Specifically, the DSC and MS signals spanning from 30 to 300 °C correspond to the desorption of interlayer confined water molecules. Typically, dehydration of highly ordered material with crystalline surface leads to sharp and narrow DSC and MS peaks. In sharp contrast, desorption of water on less ordered, amorphous surfaces causes significant DSC and MS peak broadening

© 2019 WILEY-VCH Verlag GmbH & Co. KGaA, Weinheim

(see Figure 3b,c). Such dehydration-reflected surface-orderness-decrease phenomena were also observed for mesoporous silica, large pore zeolites, and other 2D materials. One other example is MoO_3,[60] which also demonstrates promising performance serving as pseudocapacitive charge storage materials. It has been reported that the amorphous mesoporous MoO_3 shows significantly lower specific capacity compared with its crystalline form. This strongly suggests that the near-surface ion intercalation mechanisms significantly contribute to the pseudocapacitive charge storage for crystalline samples, but not to amorphous materials. Therefore, we argue that for 2D layered pseudocapacitive materials relying on intercalation mechanisms for charge storage, the near-surface crystallinity is critical to ensure high specific capacity.

Further calorimetric and computational studies are being conducted by our group to investigate the formation energetics, identification of carbonate species, and atomic-scale guest–host interaction model for the NiAl-LDH system. We will report those in subsequent publications emphasizing the physical chemistry of these NiAl-LDH materials.

4. Conclusions

In this study, we have demonstrated that the increase in the Ni/Al ratio in NiAl-LDH results in significant modification of its structural, interfacial, and electrochemical properties as a pseudocapacitive charge storage material. The increase of the Ni/Al ratio leads to a larger van der Waals gap, which enables fast ion transport and storage kinetics. Meanwhile, incorporation of more Ni atoms into the LDH layers increases the concentration of Ni redox active sites, yet sacrifices the layer crystallinity, which leads to significantly decreased pseudocapacitive charge storage capability. The high specific capacity observed when the Ni/Al ratio = 3 benefits from a balanced redox site concentration and surface crystallinity. Thus, this work demonstrates that tuning compositional factors such as the Ni/Al ratio can improve the pseudocapacitive property of transition metal layered double hydroxide materials. We anticipate that such strategies could be implemented on other transition metal–based redox active 2D structures to tune pseudocapacitive charge storage materials for better performance.

5. Experimental Section

Material Synthesis: All chemicals used were ACS reagent grade and purchased from Sigma-Aldrich. Nanopure water (18.2 MΩ cm) was used in all material synthesis experiments. NiAl-LDH samples with various Ni/Al ratios were synthesized using a hydrothermal method. The samples were denoted as NiAl-LDH-*n*, in which *n* represented Ni/Al molar ratio. In a typical synthesis, $Ni(NO_3)_2 \cdot 6H_2O$ and $Al(NO_3)_3 \cdot 9H_2O$ ([Ni] + [Al] = 1.875 mmol) with different Ni/Al ratios were mixed and dissolved in water (25 mL). The specific amount of $Ni(NO_3)_2 \cdot 6H_2O$ and $Al(NO_3)_3 \cdot 9H_2O$ added were 1.25 and 0.625 mmol for NiAl-LDH-2, 1.460 and 0.456 mmol for NiAl-LDH-3, and 1.25 and 0.365 mmol for NiAl-LDH-4. For NiAl-LDH-2, hexamethylenetetramine (HMT, 2.20 mmol) was used as the precipitant, while urea (4.13 mmol) was employed as the precipitate for NiAl-LDH-3 and NiAl-LDH-4. After 15 min reaction under stirring, the mixture was transferred into a Teflon-lined stainless-steel autoclave (50 mL) and heated at 180 °C for 72 h. The solid products were then collected by filtration, washed with nanopure water, and dried overnight in a vacuum oven maintained at room temperature.

Material Characterizations: The Ni/Al ratios of all NiAl-LDH samples were determined by inductively coupled plasma-mass spectrometry on an Agilent 7700 ICP-MS instrument. Powder X-ray diffraction patterns of all samples were collected at room temperature using a Rigaku Miniflex 600 X-ray diffractometer operated at 40 kV, 15 mA with Cu $K\alpha$ radiation (λ = 0.15418 nm). Data were acquired from 5 to 80° at 1° min^{-1} and corrected by standard material (Si). Field emission scanning electron microscope (FE-SEM) images were recorded using a field emission JEM-1400 (JEOL) electron microscope operated at 300 kV, which was equipped with a Gatan-666 electron energy loss spectrometer and an energy dispersive X-ray spectrometer. Diffuse reflectance infrared Fourier transform spectroscopy analyses were performed using a Bruker Tensor 27 IR spectrometer equipped with a Praying Mantis diffuse reflection accessory (Harrick Scientific Products). Prior to DRIFTS analysis, each sample and the background material (KBr) were subjected to pretreatment under He flow at 40 mL min^{-1} for 30 min to maximize adsorbate removal. The spectra were recorded from 4000 to 500 cm^{-1} at a resolution of 4 cm^{-1}. Raman spectroscopy analyses were also carried out on a Horiba LabRAM HR 800 spectrometer at λ = 532 nm (Ventus LP 532) equipped with a Synapse CCD (charge coupled device) detector and a Linkam CCR1000 in situ cell. X-ray photoelectron spectroscopy experiments were conducted using an ESCALAB 250Xi (Thermo Fisher) electron spectrometer with Al $K\alpha$ X-ray source (1486.6 eV).

Thermogravimetric-Differential Scanning Calorimetry-Mass Spectrometer (TG-DSC-MS) Thermal Analysis: The TG-DSC-MS analysis was performed using a Netzsch Instrument STA 449 F3 Jupiter coupled to a QMS 403 D Aeolos quadrupole mass spectrometer to quantify the H_2O and CO_2 content for each sample. The sample pellet (≈20 mg) was placed in a platinum crucible and heated from 30 to 1000 °C at 10 °C min^{-1} in nitrogen flow (20 cc min^{-1}). The evolved gas phase species was introduced from the STA to the MS. The TGA, DSC, and MS (m/z = 18 for H_2O and 44 for CO_2) data were recorded simultaneously as a function of temperature in a single experiment.

Electrochemical Measurements: The electrochemical behaviors of all samples were examined on a CHI 760E electrochemical workstation using a standard three-electrode system. An Ag/AgCl with 1.0 M KCl electrode and a platinum wire were used as reference and counterelectrode, respectively. The working electrode material contained a mixture of the as-made LDHs, acetylene black, and polytetrafluoroethylene (PTFE) with a mass ratio of 8:1:1. After overnight drying at 80 °C, the obtained electrode material slurry was coated onto a nickel grid (1 × 1 cm^2). Subsequently, it was subjected to mechanical press at 20 MPa followed by oven-drying overnight at 150 °C. The total mass of active material loaded onto each working electrode was 1–2 mg.

The cyclic voltammetry curves were recorded within the potential range of 0.0–0.6 V (vs Ag/AgCl) at various scan rates, from 5 to 100 mV s^{-1}. Galvanostatic charge/discharge measurements were carried out within the voltage range of 0.0–0.4 V with the current density ranging from 1 to 20 A g^{-1}. Electrochemical impedance spectroscopy measurements at open-circuit voltage (OCV) were performed at a series of frequency ranging from 0.01 to 100 kHz with an alternate current amplitude of 5 mV.

Gravimetric specific capacitances (C_s) of the NiAl-LDH electrodes at various scan rates were calculated by integrating the area under the CV curve of the reduction scan branch and dividing the product of sweep rate v (V s^{-1}), mass of the active material m (g), and potential window V (V).

$$C_s = \frac{\int I dV}{mVv} \tag{3}$$

The specific capacitance (C_m, F g^{-1}) was determined according to the measured galvanostatic charge/discharge plots using the equation listed below, where I (A) is the current loaded; m (g) is the total mass of the active material; Δt (s) is the discharge time; and ΔV (V) is the potential window applied on the electrodes.

$$C_m = \frac{I\Delta t}{m\Delta V} \tag{4}$$

The coulombic efficiency η of the charge storage process was calculated by the following equation, where t_c and t_d are the charge and discharge time, respectively.

$$\eta = \frac{t_d}{t_c} \times 100 \tag{5}$$

Supporting Information

Supporting Information is available from the Wiley Online Library or from the author.

Acknowledgements

This work was supported by the institutional funds from the Gene and Linda Voiland School of Chemical Engineering and Bioengineering at Washington State University. D.W. and X.G. acknowledge the fund of Alexandra Navrotsky Institute for Experimental Thermodynamics. X.Z. and C.Y. were supported by Chambroad Scholarship. H.S. acknowledges the funds from the National Natural Science Foundation of China (Grants 91634112 and 21878097) and the Natural Science Foundation of Shanghai (Grant 16ZR1408100).

Conflict of Interest

The authors declare no conflict of interest.

Keywords

composition–structure–performance relationships, energy storage, layered double hydroxides, pseudocapacitors

Received: February 25, 2019
Revised: April 29, 2019
Published online: June 11, 2019

---

[1] V. L. Pushparaj, M. M. Shaijumon, A. Kumar, S. Murugesan, L. Ci, R. Vajtai, R. J. Linhardt, O. Nalamasu, P. M. Ajayan, *Proc. Natl. Acad. Sci. USA* **2007**, *104*, 13574.
[2] F. E.-K. LMaher, S. Veronica, R. B. K. Sergey Dubin, *Science* **2012**, *335*, 1326.
[3] M. Zhao, Q. Zhang, J. Huang, F. Wei, *Adv. Funct. Mater.* **2012**, *22*, 675.
[4] H. Jiang, S. Lee, C. Li, *Energy Environ. Sci.* **2013**, *6*, 41.
[5] R. Liu, S. B. Lee, *J. Am. Chem. Soc.* **2008**, *130*, 2942.
[6] X. Xiao, T. Li, P. Yang, Y. Gao, H. Jin, W. Ni, W. Zhan, X. Zhang, *ACS Nano* **2012**, *6*, 9200.
[7] L. Mai, X. Tian, X. Xu, L. Chang, L. Xu, *Chem. Rev.* **2014**, *114*, 11828.
[8] L. Zhao, L. Z. Fan, M. Q. Zhou, H. Guan, S. Qiao, M. Antonietti, M. M. Titirici, *Adv. Mater.* **2010**, *22*, 5202.
[9] L. F. Chen, X. D. Zhang, H. W. Liang, M. Kong, Q. F. Guan, P. Chen, Z. Y. Wu, S. H. Yu, *ACS Nano* **2012**, *6*, 7092.
[10] J. Miller, P. Simon, *Science* **2008**, *321*, 651.
[11] S. Giri, D. Ghosh, C. K. Das, *Adv. Funct. Mater.* **2014**, *24*, 1312.
[12] M. Shao, F. Ning, Y. Zhao, J. Zhao, M. Wei, D. G. Evans, X. Duan, *Chem. Mater.* **2012**, *24*, 1192.
[13] D. N. Futaba, K. Hata, T. Yamada, T. Hiraoka, Y. Hayamizu, Y. Kakudate, O. Tanaike, H. Hatori, M. Yumura, S. Iijima, *Nat. Mater.* **2006**, *5*, 987.
[14] E. G. Calvo, F. Lufrano, P. Staiti, A. Brigandì, A. Arenillas, J. A. Menéndez, *J. Power Sources* **2013**, *241*, 776.
[15] W. W. Liu, X. B. Yan, J. W. Lang, C. Peng, Q. J. Xue, *J. Mater. Chem.* **2012**, *22*, 17245.
[16] Y. Tian, X. Yang, A. Nautiyal, Y. Zheng, Q. Guo, J. Luo, X. Zhang, *Adv. Compos. Hybrid Mater.* **2019**, *2*, 151.
[17] Y. Bi, A. Nautiyal, H. Zhang, J. Luo, X. Zhang, *Electrochim. Acta* **2018**, *260*, 952.
[18] X. Xiao, X. Liu, H. Zhao, D. Chen, F. Liu, J. Xiang, Z. Hu, Y. Li, *Adv. Mater.* **2012**, *24*, 5762.
[19] J. Duay, S. A. Sherrill, Z. Gui, E. Gillette, S. B. Lee, *ACS Nano* **2013**, *7*, 1200.
[20] H. Wang, H. S. Casalongue, Y. Liang, H. Dai, *J. Am. Chem. Soc.* **2010**, *132*, 7472.
[21] R. T. Vinny, K. Chaitra, K. Venkatesh, N. Nagaraju, N. Kathyayini, *J. Power Sources* **2016**, *309*, 212.
[22] S. E. Moosavifard, M. F. El-Kady, M. S. Rahmanifar, R. B. Kaner, M. F. Mousavi, *ACS Appl. Mater. Interfaces* **2015**, *7*, 4851.
[23] X. Ren, C. Guo, L. Xu, T. Li, L. Hou, Y. Wei, *ACS Appl. Mater. Interfaces* **2015**, *7*, 19930.
[24] R. R. Salunkhe, J. Tang, Y. Kamachi, T. Nakato, J. H. Kim, Y. Yamauchi, *ACS Nano* **2015**, *9*, 6288.
[25] C. C. Hu, K. H. Chang, M. C. Lin, Y. T. Wu, *Nano Lett.* **2006**, *6*, 2690.
[26] M. H. Bai, T. Y. Liu, F. Luan, Y. Li, X. X. Liu, *J. Mater. Chem. A* **2014**, *2*, 10882.
[27] D. Kong, W. Ren, C. Cheng, Y. Wang, Z. Huang, H. Y. Yang, *ACS Appl. Mater. Interfaces* **2015**, *7*, 21334.
[28] X. Liu, J. Huang, X. Wei, C. Yuan, T. Liu, D. Cao, J. Yin, G. Wang, *J. Power Sources* **2013**, *240*, 338.
[29] Y. Tao, L. Zaijun, L. Ruiyi, N. Qi, K. Hui, N. Yulian, L. Junkang, *J. Mater. Chem.* **2012**, *22*, 23587.
[30] S. Huang, G. N. Zhu, C. Zhang, W. W. Tjiu, Y. Y. Xia, T. Liu, *ACS Appl. Mater. Interfaces* **2012**, *4*, 2242.
[31] N. Yulian, L. Ruiyi, L. Zaijun, F. Yinjun, L. Junkang, *Electrochim. Acta* **2013**, *94*, 360.
[32] L. Zhang, J. Wang, J. Zhu, X. Zhang, K. S. Hui, K. N. Hui, *J. Mater. Chem. A* **2013**, *1*, 9046.
[33] G. Fan, F. Li, D. G. Evans, X. Duan, *Chem. Soc. Rev.* **2014**, *43*, 7040.
[34] M. Shao, R. Zhang, Z. Li, M. Wei, D. G. Evans, X. Duan, *Chem. Commun.* **2015**, *51*, 15880.
[35] M. Shao, F. Ning, J. Zhao, M. Wei, D. G. Evans, X. Duan, *J. Am. Chem. Soc.* **2012**, *134*, 1071.
[36] J. Xu, S. Gai, F. He, N. Niu, P. Gao, Y. Chen, P. Yang, *J. Mater. Chem. A* **2014**, *2*, 1022.
[37] X. Liu, A. Zhou, T. Pan, Y. Dou, M. Shao, J. Han, M. Wei, *J. Mater. Chem. A* **2016**, *4*, 8421.
[38] J. Fang, M. Li, Q. Li, W. Zhang, Q. Shou, F. Liu, X. Zhang, J. Cheng, *Electrochim. Acta* **2012**, *85*, 248.
[39] J. Pe, G. Mul, F. Kapteijn, J. A. Moulijn, *J. Mater. Chem.* **2001**, *11*, 821.
[40] Y. Ding, L. Xu, C. Chen, X. Shen, S. L. Suib, *J. Phys. Chem. C* **2008**, *112*, 8177.
[41] V. Rives, S. Kannan, C. Discipline, C. Salt, *J. Mater. Chem.* **2000**, *10*, 489.
[42] V. R. R. Cunha, P. A. D. Petersen, M. B. Gonc, H. M. Petrilli, C. Taviot-gueho, F. Leroux, M. L. A. Temperini, V. R. L. Constantino, *Chem. Mater.* **2012**, *24*, 1415.

© 2019 WILEY-VCH Verlag GmbH & Co. KGaA, Weinheim

[43] S. J. Palmer, R. L. Frost, G. Ayoko, T. Nguyen, *J. Raman Spectrosc.* **2008**, *39*, 395.
[44] J. Memon, J. Sun, D. Meng, W. Ouyang, *J. Mater. Chem. A* **2014**, *2*, 5060.
[45] L. Dou, H. Zhang, *J. Mater. Chem. A* **2016**, *4*, 18990.
[46] J. T. Kloprogge, L. Hickey, R. L. Frost, *J. Raman Spectrosc.* **2004**, *35*, 967.
[47] J. W. Lee, T. Ahn, D. Soundararajan, M. Ko, J. Kim, *Chem. Commun.* **2011**, *47*, 6305.
[48] L. Xiaoxi, W. Chong, D. Yibo, Z. Awu, P. Ting, *J. Mater. Chem. A* **2014**, *2*, 1682.
[49] Y. Lin, L. Ruiyi, L. Zaijun, L. Junkang, F. Yinjun, W. Guangli, G. Zhiguo, *Electrochim. Acta* **2013**, *95*, 146.
[50] F. He, Z. Hu, K. Liu, S. Zhang, H. Liu, S. Sang, *J. Power Sources* **2014**, *267*, 188.
[51] H. Wang, X. Xiang, F. Li, *J. Mater. Chem.* **2010**, *20*, 3944.
[52] J. Li, S. Tang, L. Lu, H. C. Zeng, *J. Am. Chem. Soc.* **2007**, *129*, 9401.
[53] Y. Wang, Y. Song, Y. Xia, *Chem. Soc. Rev.* **2016**, *45*, 5925.
[54] D. Du, X. Wu, S. Li, Y. Zhang, W. Xing, L. Li, Q. Xue, P. Bai, Z. Yan, *J. Mater. Chem. A* **2017**, *5*, 8964.
[55] W. Wang, N. Zhang, Z. Shi, Z. Ye, Q. Gao, M. Zhi, Z. Hong, *Chem. Eng. J.* **2018**, *338*, 55.
[56] L. Li, K. S. Hui, K. N. Hui, Y. R. Cho, *J. Mater. Chem. A* **2017**, *5*, 19687.
[57] G. Zan, W. Jun, L. Zhanshuang, Y. Wanlu, W. Bin, H. Mengjie, H. Yang, L. Qi, M. Tom, Y. Piaoping, Z. Milin, *Chem. Mater.* **2014**, *23*, 10.
[58] T. Wei, C. Chen, K. Chang, S. Lu, C. Hu, *Chem. Mater.* **2009**, *21*, 3228.
[59] M. Wang, W. Bao, J. Wang, K. Wang, J. Xu, H. Chen, X. Xia, *Sci. Rep.* **2014**, *4*, 1.
[60] T. Brezesinski, J. Wang, S. H. Tolbert, B. Dunn, *Nat. Mater.* **2010**, *9*, 146.

© 2019 WILEY-VCH Verlag GmbH & Co. KGaA, Weinheim